Ceramics International 51 (2025) 12785–12795

Contents lists available at ScienceDirect

Ceramics International

journal homepage: www.elsevier.com/locate/ceramint

Boosting the electrochemical performance of ternary metal oxide anode in lithium-ion batteries via biomass-derived carbon nanodot modification

Billur Deniz Karahan [a,b,*], Mehmet Feryat Gülcan [a]

[a] Department of Metallurgical and Materials Engineering, Istanbul Technical University, Ayazaga Campus, 34469, Istanbul, Turkey
[b] Istanbul Medipol University, Research Institute for Health Sciences and Technologies (SABITA), 34810, Beykoz, Istanbul, Turkey

ARTICLE INFO

Handling Editor: Dr P. Vincenzini

Keywords:
Carbon nanodots
transition metal oxide
Lithium-ion battery
Biowaste

ABSTRACT

Transition metal oxides deliver high capacity but demonstrate a short cycle life when they are utilized as the anode active material in lithium ion batteries. This study offers an innovative solution to this problem by designing new composite materials in which, the modification of ternary transition metal oxide by carbon nanodots is utilized. Carbon nanodots isolated from *Phoenix Dactylifera L.* seeds are used by the authors for the first time to process hydrothermally produced zinc nickel ferrite powders. Subsequently, the combination is treated in a rotating evaporator to provide a uniform mix. Then, the finished product is heated to 600 °C in air. Once these powders (ternary metal oxide from hydrothermal (Sample 1) and C-dot modified ternary metal oxide (Sample 2)) are utilized as anode active materials, Sample 2 performs 1224.74 mAh g^{-1} at the 200th cycles upon the application of 0.1 mA g^{-1} current load in cycling. Sample 2 tested under various current loads ranging from 0.1 to 2 A g^{-1} it delivers 1229.08 mAh g^{-1} at the 270th cycle. It is thus demonstrated that through careful material selection and process design it is possible to synthesize sustainable anode active materials that could withstand high current loads, with long cycle life. It is anticipated that the encouraging outcomes of this study would open up new vistas to design sustainable composite anode active materials.

1. Introduction

Rapid population growth and increased energy demands brought about by modern technology will pose problems in the creation of a sustainable future while preserving a habitable planet. Researchers are looking into sustainable solutions to ensure that people's needs are addressed while the environment is conserved. As a result, the effective use of renewable energy becomes crucial since it discourages oil-dependent growth and supports sustainable development. However, the intermittent nature of renewable energy sources highlights the critical need for the development of appropriate energy storage technology. Furthermore, these batteries power a wide range of portable electronics required for modern life, including electric vehicles.

An essential part of LIBs is the anode, which accomodates lithium ions during the charge/discharge cycle. In the state-of-the-art, graphite is mostly utilized in commercial batteries as the anode active material (AAM). However, the choice of graphite as AAM in the cell is thought to be one of the main reasons for LIB performance limitations in terms of energy and power densities due to its moderate theoretical capacity (372 mAh g^{-1}) and poor rate performance. As a consequence, scientists are attempting to either directly replace graphite with carbon-based materials of different kinds (fullerenes [1], porous carbon [2], hard carbon [3], and carbon nanodots [4]) or employ them in the creation of composite anode active material due to their superior properties (such as hydrophobicity, electrical conductivity, hardness, outstanding thermal and chemical durability, and optical qualities).

Alternatively, following the study of Tarascon et al. [5] who have proposed to use transition metal oxide as anode active material, due to their high theoretical capacities, researches on transition metal oxide anodes have gained importance. Metal ferrite is a significant candidate among various spinel structures for its potential use as an anode material in lithium-ion batteries (LIBs) as two different metal cations in a single-crystal structure results in distinct properties. Li et al. [6] have stated that among metal ferrites, nanosized zinc ferrite ($ZnFe_2O_4$) stands out as it may have additional reversible alloying reaction with Li, providing a theoretical specific capacity of 1000 mAh g^{-1} [7]. According to Yao et al. [7], zinc ferrite is a promising candidate for LIB anodes due to its non-toxicity, environmental friendliness, structural stability, and low cost. The possible reactions of $ZnFe_2O_4$ with Li is investigated in previous studies [8–14]. Although the high theoretical capacity of zinc

* Corresponding author. Department of Metallurgical and Materials Engineering, Istanbul Technical University, Ayazaga Campus, 34469, Istanbul, Turkey.
E-mail address: bdkarahan@itu.edu.tr (B.D. Karahan).

https://doi.org/10.1016/j.ceramint.2025.01.117
Received 6 October 2024; Received in revised form 5 January 2025; Accepted 7 January 2025
Available online 7 January 2025

ferrite attracts the attention, its low electrical conductivity causes poor cycle retention. These drawbacks result in poor rate performance and cycle retention capabilities, which limit its wide-spread application in LIBs. As a solution, nanoengineering [15] has been suggested to shorten the Li diffusion length in the solid particle, and composite formation [16] has been put forward to solve the problem of volumetric expansion and electrical conductivity [17]. Therefore, understanding the structure and electrochemical properties of $(Ni_{1-x}Zn_x)Fe_2O_4$ is crucial [14].

$$Zn^0 + Li^+ + e^- \leftrightarrow LiZn \quad \text{(Eq1)}$$

$$ZnFe_2O_4 + 0.5\,Li^+ + 0.5e^- \rightarrow Li_{0.5}ZnFe_2O_4 \quad \text{(Eq2)}$$

$$Li_{0.5}ZnFe_2O_4 + 1.5\,Li^+ + 1.5e^- \rightarrow Li_2ZnFe_2O_4 \quad \text{(Eq3)}$$

$$Li_2ZnFe_2O_4 + 6Li^+ + 6e^- \rightarrow 4Li_2O + Zn + 2Fe \quad \text{(Eq4)}$$

$$2Fe + 3Li_2O \leftrightarrow Fe_2O_3 + 6Li^+ + 6e^- \quad \text{(Eq5)}$$

$$Zn + Li_2O \leftrightarrow ZnO + 2Li^+ + 2e^- \quad \text{(Eq6)}$$

Nevertheless, like other TMOs, $(Ni_{1-x}Zn_x).Fe_2O_4$ anode usually suffers from poor electrical conductivity due to the strong atomic binding energy and unstable structure because of the large volume changes occurred in cycling [7]. These drawbacks result in poor rate performance and cycle retention capabilities, which limit its wide-spread application in LIBs. Recently, nanoengineering [15] has been suggested to shorten the Li diffusion length in the solid particle, and composite formation [16] has been put forward to solve the problem of volumetric expansion and electrical conductivity [17]. Chao et al. [18] use the metal oxides with carbon derivatives and report that copper oxide with graphene nanodot could recover itself even after 30C. Then Nan et al. [19] decorate LTO with carbon quantum dots (CQDs) and Jiang et al. [20] synthesize N-doped Carbon dots with $FeCO_3$ by hydrothermal method. The finding shows that the CND improves the electrochemical performance as it limits the agglomeration of particles. Despite these remarkable developments in material science, it is challenging to guarantee the sustainability of the final product because the anode active material synthesis process uses synthetically produced starting materials that have a significant negative influence on the environment. This fact detrimentally impacts how environmentally friendly the manufacturing process is. Therefore, inventing a method for enhancing the environmentally friendly features of TMO-based AAM for LIBs is essential.

A recent development in nanotechnology and nanoscience, carbon dots (CND) have garnered a lot of attention because of their great photostability, biocompatibility, affordability, and fluorescent qualities. They can also be produced from organic materials, including biowaste. Therefore, there is a growing interest in producing CND utilizing scalable and low-cost production techniques. This concept allows for the valorisation of waste, which not only reduces environmental pollution but also promotes economic growth. Within this context, Krajewski et al. [21] modified lithium titanate (LTO) with bio-derived (i.e.carrot juice) carbon nano dot, resulting in superior electrochemical performance, eventually.

In this study, first time in the open literature, the seeds of *Phoenix Dactylifera* are used as the initial material to prepare carbon dots. As the annual production of the seed is reported to be over 8 million [22], a substantial quantity of *Phoenix Dactylifera* seeds may be employed as carbon sources to synthesize diverse polymers or nanostructures [23]. Previously the use of *Phoenix Dactylifera* seed as cellulose source has been reported [24]. Studies on the use of CNDs solely in supercapacitors, lithium-ion batteries, and sodium-ion batteries have been also conducted: Song et al. [4] report the direct use of carbon dots as anode active material and its performance is found to be poor due to its limited capacity and conductivity. Therefore, in this work, for the first time in the literature, CND—which are derived from *Phoenix Dactylifera* L. *Seed*, being classified as a biowaste—are used to modify zinc ferrite $((Ni_{1-x}Zn_x).Fe_2O_4)$ in order to be used as AAM in LIB. The results show that the application of CND efficiently prevents the agglomeration of nanosized zinc ferrite particles, resulting in higher specific capacity and rate capability.

2. Experimental

2.1. Raw materials used in the experiments

Iron sulfate heptahydrate, nickel sulfate hexahydrate, zinc sulfate heptahydrate and hydrogen peroxide (vol. %50) of technical grade were used. Ammonium hydroxide (~25 % NH_3 basis) was of Merck quality.

Date seeds *(Phoenix Dactylifera* L.*)* were obtained from the local market.

2.2. Material synthesis

2.2.1. Carbon nanodot synthesis

Date seeds (*Phoenix Dactylifera* L.*)* were heat treated at 300 °C for 2 h in an air atmosphere. Subsequently, 1 g of the heat-treated date seeds was ground in a planetary ball mill (Retsch PM100) for 5 h at 400 rpm. To achieve a uniform dispersion in the solvent, 200 mg of this finely carburized powder was added to 10 mL of water and the mixture was processed in an ultrasonic bath filled with ice water. Next, 20 mL of 30 % hydrogen peroxide (H_2O_2) was added into the solution which was heated to 80 °C. Following 10 min of vigorous mechanical stirring, an extra 5 mL of a 30 % H_2O_2 solution was added to the solution. In less than 40 min, H_2O_2 was added four times in to the micture. When the reaction was accomplished, the mixture contained 40 mL of H_2O_2. Finally, the solution was stirred for three more hours. The liquid was then boiled to eliminate any excess H_2O_2, and carbon nanodots were collected by diluting it with distilled water [25].

2.2.2. Ternary transition metal oxide synthesis

5 mmol each of iron, zinc, and nickel sulfates were mixed together for an hour at room temperature. After adding NH_4OH (14 M) to bring the mixture's pH to 10, the mixture was agitated for 3 h, then placed into the hydrothermal reactor (at 150 °C for 24 h). Once the reaction was completed, the particles were collected using a centrifuge with two cycles of washing with ethanol, then water at 4000 rpm for 20 min each. The precipitate obtained was then calcined for 3 h at 800 °C in air. The produced sample was labeled as Sample 1.

2.2.3. Carbon dots modified ternary transition metal oxide synthesis

Firstly, Sample 1 (as defined in section 2.2.2. Ternary transition metal oxide synthesis) and the carbon nanodot solution (as defined in section 2.2.1.Carbon nanodot synthesis) were mixed in Buchi Rotavapor® R-300. Then, the mixture was heated under vacuum (500 mbar, 90 °C, 45 min 80 rpm). Once the solvent was completely removed, the precipitate was dried under a vacuum overnight (110 °C 12 h). Then, Sample 2 was prepared by heat-treating the mixture in air atmosphere (at 600 °C for 4 h) (see Supp.Fig. S1).

2.2.4. Electrode synthesis

Samples 1 and 2 were used as anode active material (AAM). The slurry's composition had 80%wt active powder (Sample 1, Sample 2), 10%wt PVDF (polyvinylidene fluoride, MTI HSV900) and 10%wt Super P conductive (TICMAL) dissolved in NMP (N-Methyl-2-pyrrolidone, Merck). All compounds were blended in a Thinky ARE250 to create electrode slurries. Dr. Blade was utilized followed by casting slurries onto copper foils that were 15 μm thick. After 8 h at 80 °C and 16 h at 120 °C under vacuum drying, the electrodes were cold-rolled to a thickness of less than 30 μm.

CR2032 coin-type half-cells were assembled in an argon-filled glovebox (MBRAUN, Labmaster; $H_2O < 0.1$ ppm $O_2 < 0.1$ ppm) in order to

assess the electrochemical performances of the electrodes. Each cell was composed of the following components: an electrolyte (Merck Battery Grade electrolyte solution, 1 M $LiPF_6$ dissolved in ethylene carbonate-dimethyl carbonate, EC: DMC 1: 1), a separator (Celgard 2400), a counter electrode (Li metal foil), and a working electrode (Sample 1, Sample 2). The mass loading of active materials was 0.3 mg/cm^2 in average.

2.3. Structural and morphological characterization

2.3.1. Ternary transition metal oxide based powders

X-ray diffractometer (Bruker D2 Phaser, Cu Kα) was used to examine structural characteristics with 2θ = 10–70° scanning at a rate of 0.02°/sec. Morphological investigations of Samples 1, 2 as well as ex-situ analysis of each electrode after 1st charge and 1st discharge reactions were performed via Zeiss Gemini 500 Scanning Electron Microscope. For detailed characterization of carbon nanodots, Transmission Electron Microscopy (TEM, by JEOL JEM 2100Plus) was used. To determine existing bonding, X-ray photoelectron Spectroscopy (XPS) was performed by Thermo K-Alpha.

2.3.2. Carbon nanodot analysis

UV–VIS spectroscopy was used to assess the optical characteristics. Measurements of absorbance spectra were conducted in the range of 300–700 nm, while fluorescence was measured at various excitation wavelengths using the SpectraMax i3 Multi-Mode Platform from Molecular Devices.

2.4. Electrochemical characterization

2.4.1. Galvanostatic testing

Neware battery analyzer was used for measurement. At a current load of 100 mA g^{-1}, each electrode's cycling performance was assessed between 10 mV and 3 V (vs Li/Li$^+$). The rate performance of each electrodes were then recorded when varying current loads (ranging from 100 mA g^{-1} to 2000 mA g^{-1}) were applied on each electrode.

2.4.2. Potentiostatic testing

Gamry 1000E was used as potentiostat. Cyclic voltammograms (CV) of Samples 1, 2 were recorded in half-cells in order to examine the lithiation reactions. For the first four cycles, CV curves were scanned at a rate of 0.2 mV s^{-1} between 10 mV and 3 V (versus Li/Li$^+$).

Additionally, impedance measurements were done at discharged states (vs Li/Li$^+$) in the half-cell. The Gamry Interface 1000E was used to obtain electrochemical impedance spectra (EIS) and Gamry Echem Analyst was used for modelling.

3. Results and discussion

3.1. Structural, morphological and chemical characterizations

3.1.1. Carbon nanodots

Carbon nanodots are derived from *Phoenix Dactylifera* L. *seeds* (Images taken from different stages of the process are given in Figs. S2a–f) following the '*chemical oxidation*' principles [25–27]. It is known that the date seeds contain 22.5–80.2%wt. dietary fibers (cellulose, hemicellulose, and lignin) and other ingredients [24]. As mentioned in the experimental section, seeds are first washed then treated in 300 °C in air ambient to remove proteins, oils etc. and carburize the waste [28]. 300 °C is chosen for carburization following Babiker et al. [29] who claim that high temperatures (200–700 °C) are required for the breakdown of lignocellulosic components; and, Kamal et al. [30] report that *Phoenix Dactylifera L.* seeds had minimal lignin content. Therefore, it is anticipated that 300^{0}C would be adequate to carburize seeds of *Phoenix Dactylifera L.*

In the fabrication of carbon nanodots, carburized powder is treated with H_2O_2 since OH^- radicals in H_2O_2 could selectively oxidize carbon chain and form CO_2 and H_2O at moderate temperature (80 °C), resulting in the formation of carbon nanodots suspension, eventually [25]. The absorbance graph of CNDs (Fig. S3a) shows that a peak at 300 nm is associated with the π-π* graphitic electron transition. Additionally, peaks associated with the n-π* transition and the π conjugated aromatic system that are displayed by carbonyl and other oxygen-containing compounds are also noted [31]. Fig. S3b reveals that carbon nanodots based on cellulose have similar spectra [31]. A minor change in the spectra's various excitation wavelengths is also visible in Fig. S3b. The emission peak red-shifts from 453 nm to 540 nm as the excitation wavelength varies from 290 nm to 405 nm, are attributable to surface energy traps, radiative recombination of electrons and holes, and maybe polycyclic aromatic molecules inside CNDs [32]. Moreover, the excitation wavelength-dependent fluorescence emission behavior of CNDs is frequently caused by surface defects rather than the band gap transition of conjugated π domains, which is believed to be crucially important for high rate anode [32,33].

3.1.2. Carbon dot modified ternary transition metal oxide based powders

For the synthesis of ternary oxide, equal stochiometric amount of metal sulfate salts (mentioned in experimental section) and ammonium hydroxide (NH_4OH) have been used to prepare the hydrothermal solution. Ammonium hydroxide releases OH^- ions and increases pH of the solution which leads to the formation of metal hydroxide according to the literature (Eq(s 7)–(12)) [31–34].

$$NH_4OH \leftrightarrow NH_4^+ + OH^- \quad \text{(Eq7)}$$

$$FeSO_4 \rightarrow Fe^{2+} + SO_4^{2-} \quad \text{(Eq8)}$$

$$Fe^{2+} + 2OH^- \rightarrow Fe(OH)_2 \quad \text{(Eq9)}$$

$$Zn^{2+} + 4OH^- \rightarrow Zn(OH)_2^{2-} \quad \text{(Eq10)}$$

$$Zn(OH)_2^{2-} \rightarrow ZnO + H_2O + 2OH^- \quad \text{(Eq11)}$$

$$Ni^{2+} + 2OH^- \rightarrow Ni(OH)_2 \quad \text{(Eq12)}$$

In this work, hydrothermal reaction conditions (temp (150 °C), duration (24 h), filling ratio (vol/vol%100), metal salt molarity (0.025 M)) are chosen to obtain submicron sized ternary ferrite particles formation (The experimental parameters and outcomes where the best results were attained are presented here; the actual results of the tests conducted for optimization are not provided in this manuscript). According to Velmurugan et al. [35], a ternary oxide can form in an alkaline medium under heating conditions (150 °C) of hydrothermal reaction.

$$(1-x)Ni(OH)_2.\ xZn(OH)_2.\ 2Fe(OH)_3 \xrightarrow{\text{under heating}} Ni_{1-x}Zn_xFe_2O_4.nH_2O \quad \text{(Eq13)}$$

Hydrothermal reaction followed by heat treatment reveals that (Ni, Zn)Fe_2O_4 phase is formed following Eq. (13). The result shows that the powder has revers spinel structure. Reddy et al. [14] have reported that such structure performs low capacity but good retention due to hybrid structure. In the unit cell, nickel and iron in a spinel structure have no order in their positions and Zn positions mostly at the surface of the particle [36], thus the heat treatment of the particle at 800 °C causes partial oxidation of Zn followed by the formation of (Ni, Zn)Fe_2O_4 and ZnO (Sample 1).

A scrutiny look in XRD reveals that peaks related to (Ni, Zn)Fe_2O_4 (00-008-0234) (2Θ = 18.28, 30.02, 35.52, 36.99, 42.95, 53.5, 57.17, 62.57 and 74.04), and ZnO (2Θ = 31.94, 34.43) are noted in both samples. All samples have spinel structure in agreement with the literature [14,38,40] (Fig. 1a–c).

According to SEM images (Fig. 2a–c), both samples have pseudo

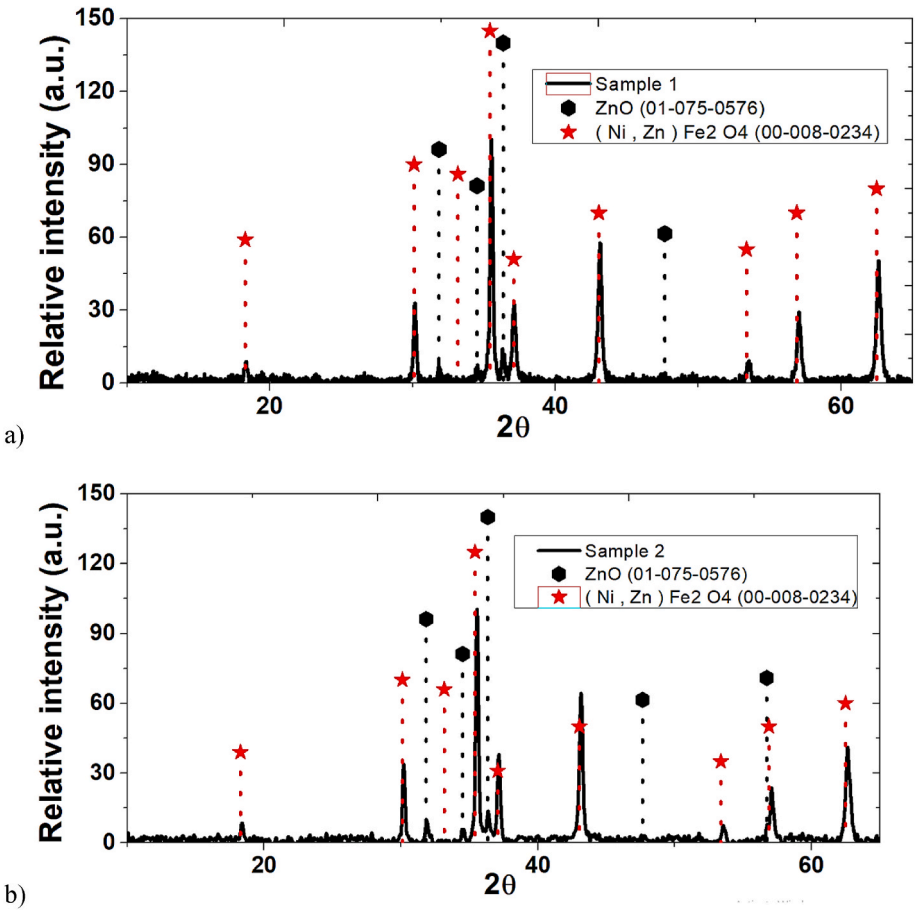

Fig. 1. XRD investigations a) Sample 1 b) Sample 3.

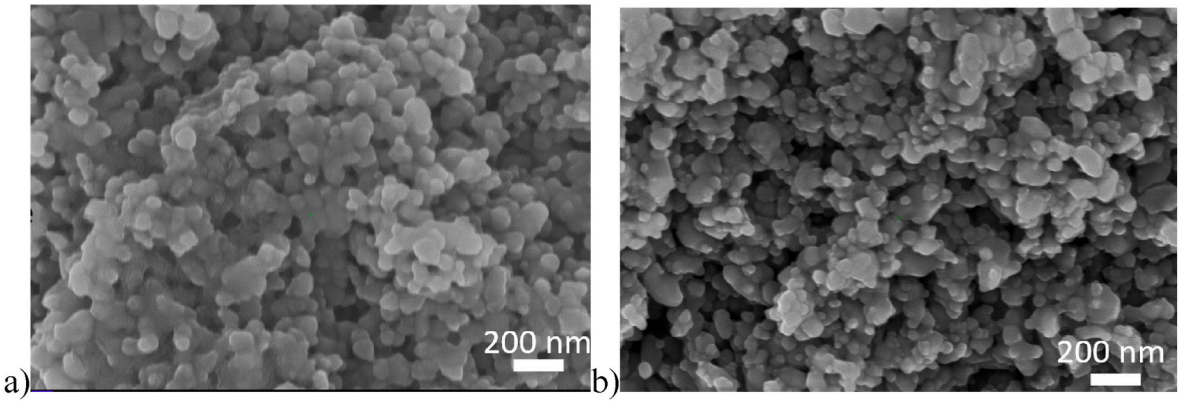

Fig. 2. SEM images a) Sample 1 b) Sample 2.

cubic morphology and in both samples particle dimensions are under 100 nm. A scrutiny look reveals that carbon nanodot treatment inhibits particle agglomeration, observed elsewhere [4].

To study the distribution of CND in the oxide powder, TEM examination is performed on Sample 2. Fig. 3a gives general image of Sample 2 which agrees with the SEM image (Fig. 2b). Fig. 3b proves the prevalence of zinc nickel ferrite in the powder as (111) plane of $(Ni,Zn)Fe_2O_4$ is clearly seen. Moreover, ZnO presence on particle surface is revealed in Fig. 3c. Swaminathan et al. have explained the formation of ZnO thin film on the surface [36] due to volatilization of zinc [38]. (220) plane is also observed on the same particle core (Fig. 3c). In Fig. 3d, (111) plane is observed for $(Ni,Zn)Fe_2O_4$ which is the most preferred orientation due to highest theoretical intensity value according to 00-008-0234 card. On the surface of particles, there are some dot like clusters which demonstrate heterogenous accumulation for carbon nanodots on ternary oxide particle. According to Fig. 3d and e, carbon nanodots are marked and measured for their diameter which are 1 ± 0.2 nm. The size of carbon nano particles is similar with Hu et al. study [25] which have been used H_2O_2 treatment on coal particles.

XPS survey (Fig. 4a–e) has been performed to determine bonding types of elements in carbon dots modified sample (Sample 2). The peak at 854.9 eV shows the existence of Ni2p2/3 which reveals the existence of Ni^{2+} in the spinel ferrite system [39]. Zinc exhibits peaks at 1021.40 eV and 1044.37 eV which are ascribed to Zn2p2/3 and Zn2p1/3 related

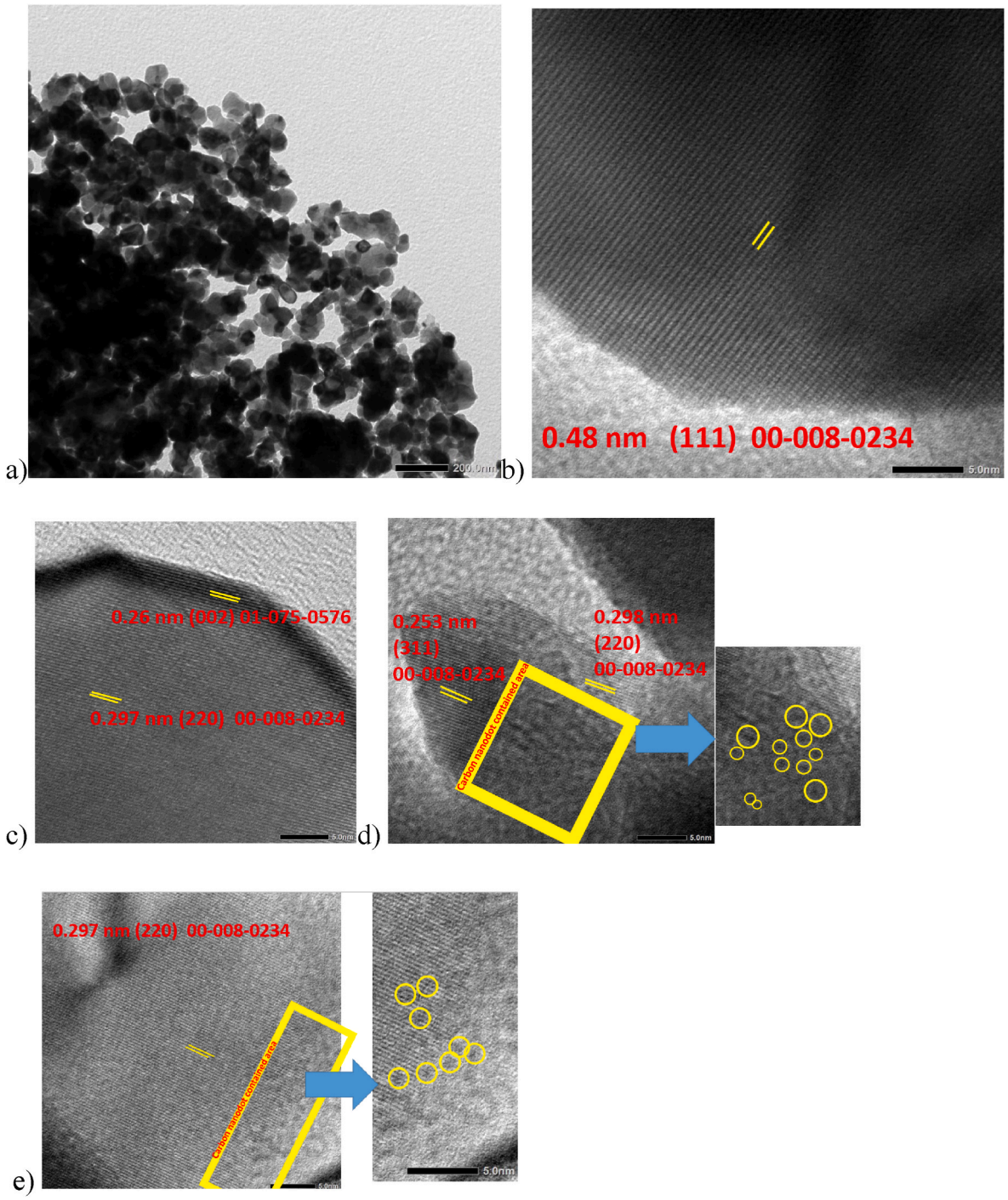

Fig. 3. TEM analysis a)general imaging b) (111) plane for (Ni,Zn)Fe_2O_4 c) (220) plane for (Ni,Zn)Fe_2O_4 and (002) plane for ZnO d) (311) and (220) planes for (Ni, Zn)Fe_2O_4 and accumulated carbon nanodots on the particle surface e) (220) plane for (Ni,Zn)Fe_2O_4 and accumulated carbon nanodots on the particle surface.

to the oxidation state of Zn^{2+}, in the ferrite [40], and in the zincite, respectively. Iron has two peaks at 724.26 eV and 710.8 eV which correspond to Fe2p1/3 and Fe2p2/3, respectively [41]. Oxygen peak is deconvoluted: the peak at 529.4 eV corresponds to lattice oxygen [42]. 529.2 eV and 529.6 eV are associated with Fe-O and Zn-O, respectively [43]. Fe-O and Zn-O binding energy values are close to 529.4 eV which result from the redistribution of tetrahedral and octahedral sites. Peaks related to carbon are also deconvulated: at 531 eV a peak showing the oxygen binding to carbon nanodot is noted [44]. Moreover, at 532.19 eV a peak related to C–O–C/C–OH binding is seen. When the peak of C is deconvulated, three peaks are characterized: the peak at 284.45 eV reveals the presence of C=C (sp2)/C-C (sp3) [45], while the peak at 286.54 eV exhibits the C-OH binding [46], and the peak at 288.44 eV demonstrates the existence of C=O binding [47]. Those peaks all reveal the carbon nanodots' existence after heat treatment of Sample 2 in air, with no further reduction of metal oxide in the powder. Therefore, no peak related to metal formation (Zn,Fe,Ni) is noted in Sample 2, which is taken to mean that treatment of the ternary metal oxide with C-dots in 600 °C air atmosphere does not lead to reduction reaction.

Additionally, Raman analysis has been performed for further investigation (Fig. 4f). There are peaks related to Zn-O (at 317 cm^{-1}) [48], Ni-O (at 475 cm^{-1}) [49], Fe-O (at 669 cm^{-1}) [50], D-band (at 1345

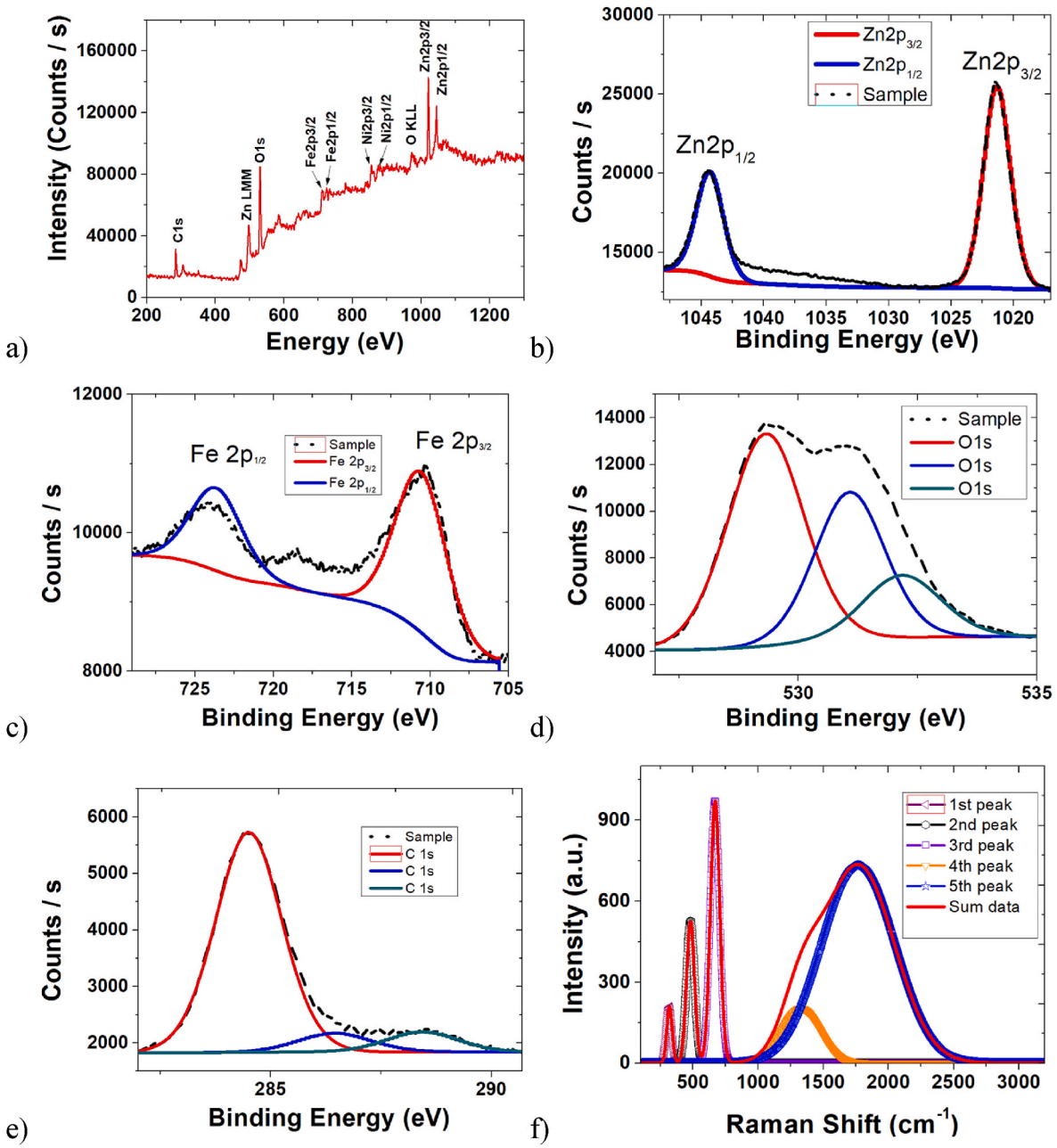

Fig. 4. XPS survey for Sample 2 a) XPS spectrum b)Zn spectrum c) Fe spectrum d) O spectrum e) carbon spectrum. f) Raman spectrum for Sample 2.

cm^{-1}) [51] and C=O stretching bond (at 1750 cm^{-1}) [52]. These analyses are further proof for the existence of carbon dots and metal oxide formation [53].

3.2. *Electrochemical performances of modified ternary metal oxides*

To determine the electrochemical properties of both samples, half cells are assembled and electrodes are tested between 10 mV and 3 V (vs Li) under a current load of 0.05 A g^{-1} for 2 cycles then 0.1 A g^{-1} for 200 cycles. Sample 1 and Sample 2 demonstrate 538.07 $mAhg^{-1}$ and 1933.9 mAh g^{-1} as 1st discharge capacities when 50 mA g^{-1} current load is applied. After the 2nd cycle at 50 mA g^{-1}, Sample 1 and Sample 2 deliver 348.4, and 1235 mAh g^{-1} discharge capacities with 99.0 % and 99.99 % capacity retention after 200 cycle. Fig. 5a demonstrates that Sample 1 shows a progressive decrease whilst Sample 2 exhibits first a decrease followed by an increase in the capacity. Such fluctuations in the cycle performance of Sample 2 is seen in nanometers-sized TMO anodes. Keller et al. [54] have argued that the fluctuation is related to the intermetallic formation occurring in discharge. Moreover, formation of SEI could cause capacity fluctuation during cycling [55,56]. Song et al. [4] have mentioned that carbon nanodot could generate internal stresses in cycling and limit the dramatic effect (such as pulverization, delamination etc) of volumetric changes. When looking for performance under different current loads, Sample 1 reveals the poorest performance. Unlike Sample 1, Sample 2 delivers superior capacity than graphite and LTO: 540 mAh g^{-1} at 1 A g^{-1} and 450 mAh g^{-1} at 2 A g^{-1} (Fig. 5b). When the capacity voltage profiles of samples are studied, 2 plateaus at the 1st discharge become apparent around 0.7 V and 0.55 V. According to Wang et al. [57], the initial discharge profile indicates the lithiation of (Ni, Zn)Fe_2O_4, while the second plateau at 0.55 V is attributed to the lithiaton of metal oxide (i.e. NiO and ZnO) with Li [58,59] (see Fig. 6).

$$Ni_xZn_{1-x}Fe_2O_4 + 8\,Li^+ + 8e^- \rightarrow x\,Ni + (1-x)Zn + 2Fe + 4\,Li_2O \quad \text{(Eq14)}$$

After the 1st discharge, lithiation reactions are realizedaccording to

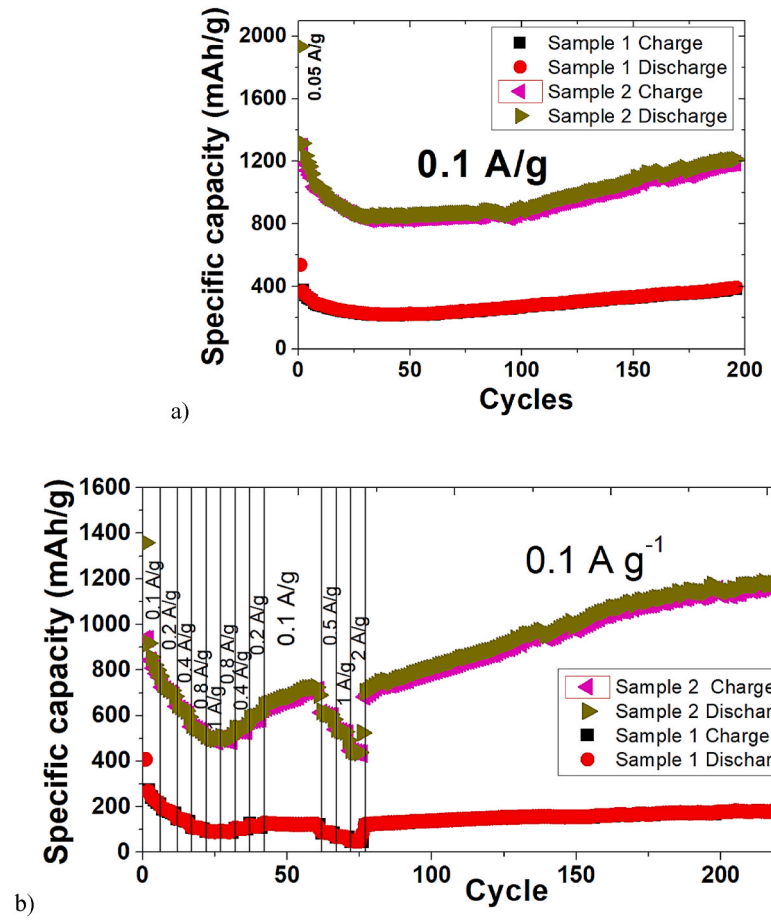

Fig. 5. The capacity cycle graps of all samples between 10 mV and 3 V a) at 0.1 Ag^{-1} current load b) under different current load: rate test performance.

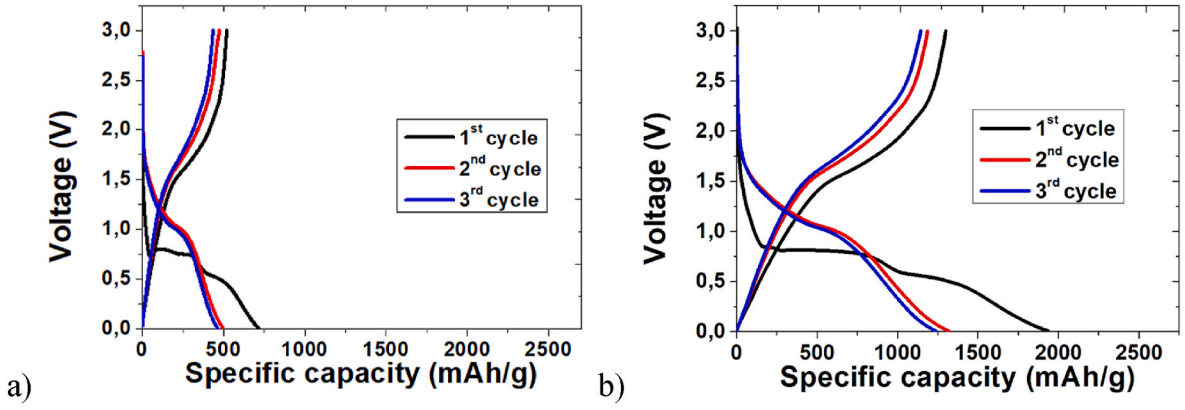

Fig. 6. Capacity-Voltage curves for a) Sample 1 b) Sample 2.

Eq(15)–(17) [37]:

$$x\,Ni + (1-x)Zn + Li_2O \leftrightarrow xNiO + (1-x)ZnO + 2Li^+ + 2e^- \quad \text{(Eq15)}$$

$$Fe + Li_2O \leftrightarrow FeO + 2Li^+ + 2e^- \quad \text{(Eq16)}$$

$$2Fe + 3Li_2O \leftrightarrow FeO + 6Li^+ + 6e^- \quad \text{(Eq17)}$$

To study the surface reaction of each electrode, CV test is applied. Fig. 7a and b show that each electrode has peaks at 0.25, 0.3 and 0.7 V during the 1st cathodic scan of CV test. The cathodic peaks are believed to be related to the reduction of the electrolyte as well as that of the zinc ferrite (Ni, Zn)Fe_2O_4 [37], as defined previously [60,61] (Fig. 7a and b).

The comparison of the 1st CV curve reveals that apart from the existence of carbon dots, no additional peak is noted but the peak intensities are larger in sample 2. This fact verifies that carbon dots do not react with Li, but promote the SEI formation as well as the reduction of zinc ferrite (Ni, Zn)Fe_2O_4. In the 1st anodic scan, a peak (around 1.7 V) is presented which is related to oxidation of ternary metals in the structure. Following 1st cycle, both electrodes reveal changes in peak positions and intensities. From 2nd to 4th cycles, high reversibility is noted on the surface reaction of each electrode following Eq (14). The cathodic peaks noted at 1 and 1.3V show structural rearrangement [37], in anodic scan, the oxidation peak at 1.7V reveals Zn^0 and Fe^0 oxidation [37].

Fig. 8a–c depict the EIS data collected for Samples 1 and 2, and the

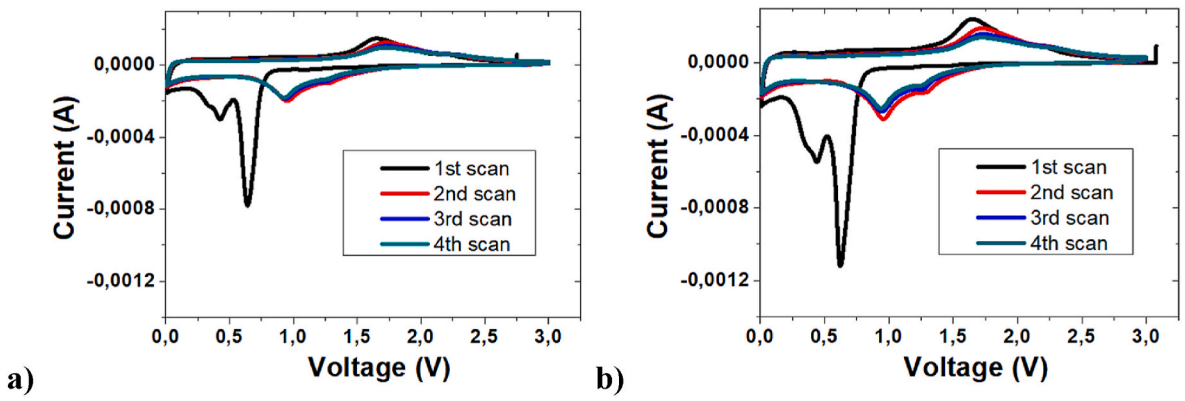

Fig. 7. CV curves for a) Sample 1 b) Sample 2.

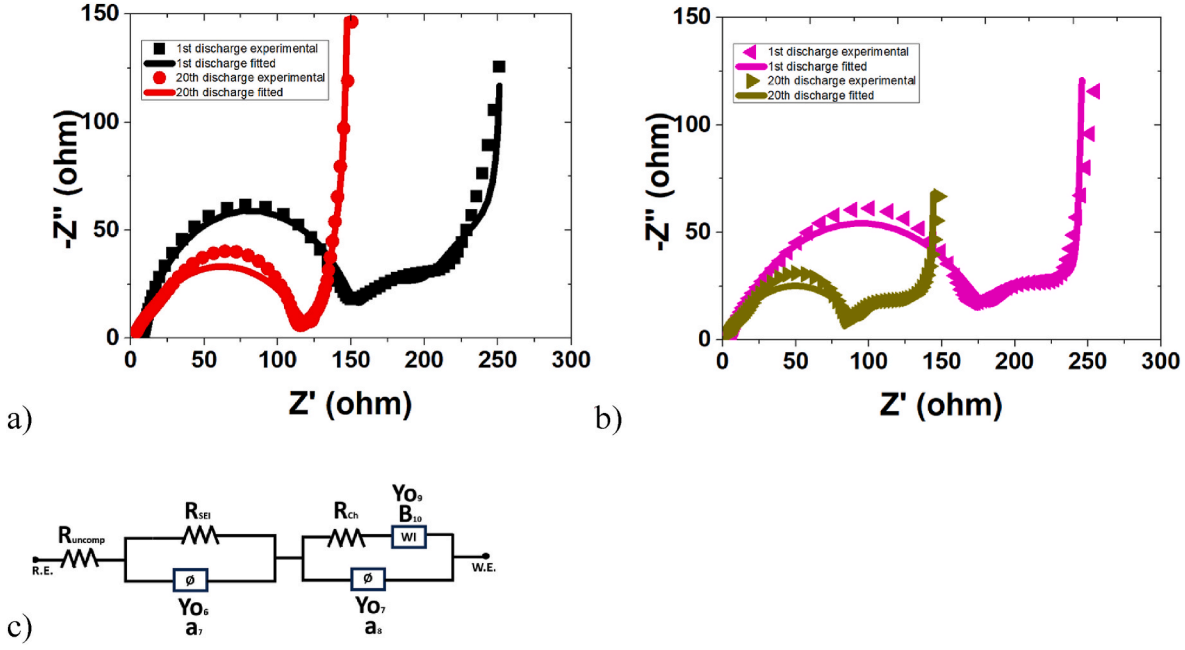

Fig. 8. EIS test results of a)Sample 1 and b)Sample 2 at 1st discharge and 20th discharge states.c) Equivalent circuit.

equivalent circuit models, respectively. The morphologies of the EIS spectra are similar, consisting of two semicircles and one slope line (Fig. 8a and b). An intercept at high frequency is related to the ohmic uncompensated resistance (R_{uncomp}). The first semicircle at high frequency corresponds to SEI, whereas the second semicircle represents charge transfer at the electrode/electrolyte interface. The inclined line at low frequency corresponds to the Warburg impedance (W), which denotes the solid state diffusion of Li^+ ions into the anode active material. Fig. 8a and b shows that both samples have low initial uncompensated ohmic resistance (R_{umcomp}) values in the first and twentieth discharged states. This evidently demonstrates that both half-cells are successfully assembled, with a low internal resistance loss. In both samples, SEI (R_{SEI}) and charge transfer (R_{Ch}) resistances are reduced from the 1st to 20th cycles. This is explained by the presence of a stable SEI film formation at the electrode/electrolyte interface. A comprehensive examination reveals that the charge transfer resistance in sample 2 modified with C-dot is lower than sample 1 in both 1st and 20th cycles. This is explained by the fact that C-dot modification makes charge transfer easier, which improves Sample 2's rate performance, eventually. Data from EIS are compatible with galvanostatic test results.

Ex-situ images for electrodes after charge and discharge are investigated for further explanation. In Sample 1, some swollen particles are noted and cracks are observed after the 1st discharge reaction (Fig. 9a). Then in charged state of Sample 1, small particles are observed with partial agglomeration forming clusters. Unlike Sample 1, Sample 2 has no crack formation in the discharged state as C-dot existence inhibits the agglomeration of particles and controls the volumetric expansion. Sample 2 at 10 mV has a homogenous electrode surface. After charge to 3 V, Sample 2 has a more homogenous surface texture.

Ex-situ investigations shows that carbon nano dot modification leads to better SEI formation than pristine sample. Song et al. [4] mentioned that carbon nano dots have a protective role during lithiation and delithiation. According to ex-SEM images (Fig. 9a–d), Sample 2 has carbon nanodots protective effect during lithiation and delithiation.

4. Conclusion

This article describes an alternative process for producing high-energy density anode active material for lithium-ion batteries. Initially, a ternary metal oxide is prepared using a hydrothermal process (Sample 1). This oxide powder is modified with carbon dots generated from *Phoenix Dactylifera L.* Seed (Sample 2) to create a unique composite in an environmentally benign manner.

The material selection and process design approaches described in

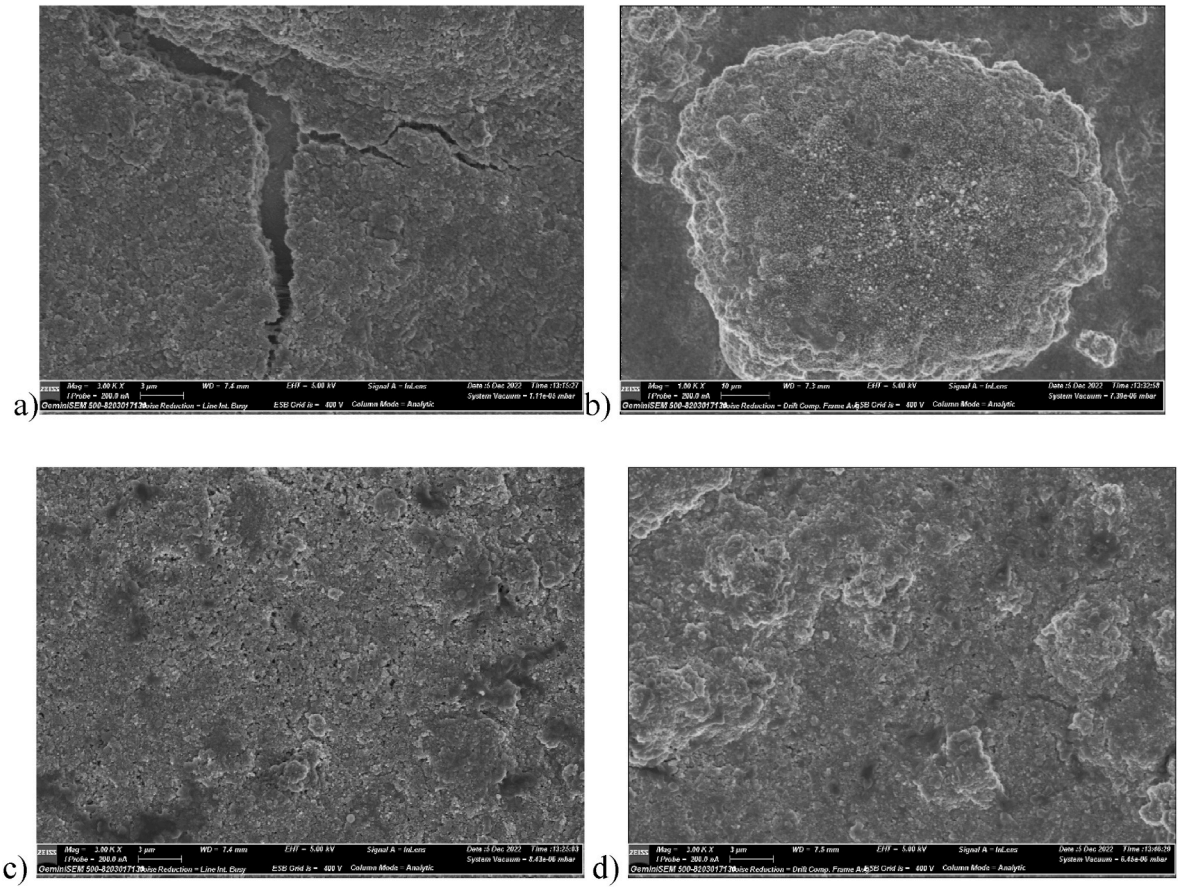

Fig. 9. Ex-Situ images of electrodes after 1st discharge at 10 mV (vs Li/Li^+) a) Sample 1, c) Sample 2; and after 1st charge at 3 V (vs Li/Li^+) b) Sample 1, d) Sample 2.

this work are novel, and the outcomes are remarkable, as outlined below.

- For the first time, carbon dots were produced from *Phoenix Dactylifera L.* Seed using a chemical oxidation process. A strong PL emission peak located at 460 nm was observed with an excitation wavelength of 360 nm.
- For the first time, the resulting C-dot was integrated into the ternary metal oxide using a rotary evaporator. TEM results showed that by treating C-dots and ternary metal oxide together in a rotary evaporator, an integration of C-dots to the metal oxide was achievable.
- The heat treatment of Cdot-modified ternary metal oxide resulted in reduced particle size as the carbon nanodot in the composite inhibited agglomeration.
- C-dot modified ternary metal oxide was used as the anode active material, and its performance was tested galvanostatically. Thanks to the presence of these C-dots, the charge transfer resistance in ternary metal oxides was decreased and the SEI formation was differentiated, resulting in better capacity, higher cycle retention and improved performance under high current loads

CRediT authorship contribution statement

Billur Deniz Karahan: Writing – original draft, Supervision, Resources, Methodology, Investigation, Conceptualization. **Mehmet Feryat Gülcan:** Writing – original draft, Visualization, Investigation.

Declaration of competing interest

The authors declare the following financial interests/personal relationships which may be considered as potential competing interests: BD Karahan used to work at Istanbul Medipol University which sponsored the realization and characterization of the experiments.

Istanbul Technical University is the current affiliation of the corresponding author.

Acknowledgments

The authors greatly acknowledge Istanbul Medipol University Regenerative and Restorative Medicine Research Center for allowing the use of SEM and XRD in characterizations. The authors thank Prof. Dr. Talip Alp for editing the manuscript and Istanbul Medipol University for sponsoring the realization and the characterization of the experiments. BD Karahan used to work at Istanbul Medipol University which sponsored the realization and characterization of the experiments. Istanbul Technical University is the current affiliation of the corresponding author.

Appendix A. Supplementary data

Supplementary data to this article can be found online at https://doi.org/10.1016/j.ceramint.2025.01.117.

References

[1] J.A. Teprovich, J.A. Weeks, P.A. Ward, S.C. Tinkey, C. Huang, J. Zhou, R. Zidan, P. Jena, Hydrogenated C60 as high-capacity stable anode materials for Li ion batteries, ACS Appl. Energy Mater. 2 (2019) 6453–6460, https://doi.org/10.1021/acsaem.9b01040.

[2] L. Han, S. Kang, X. Zhu, J. Li, Q. Wang, X. Jia, High-performance lithium-ion capacitors produced by atom-thick carbon cathode and nitrogen-doped porous carbon anode, Energy Fuel. 35 (2021) 16894–16902, https://doi.org/10.1021/acs.energyfuels.1c02509.

[3] S.C. Dey, B. Worfolk, L. Lower, W.J. Sagues, M.R. Nimlos, S.S. Kelley, S. Park, Phenolic resin derived hard carbon anode for sodium-ion batteries: a review, ACS Energy Lett. 9 (2024) 2590–2614, https://doi.org/10.1021/acsenergylett.4c00688.
[4] T.B. Song, Z.H. Huang, X.Q. Niu, J. Liu, J.S. Wei, X.B. Chen, H.M. Xiong, Applications of carbon dots in next-generation lithium-ion batteries, ChemNanoMat 6 (2020) 1421–1436, https://doi.org/10.1002/cnma.202000355.
[5] P. Poizot, S. Laruelle, S. Grugeon, L. Dupont, J. Tarascon, (2000 Nature) Nano-Sized Transition-Metaloxidesas, 2000, p. 407.
[6] Y. Li, Y. Meng, X. Liu, M. Xiao, Q. Hu, R. Li, X. Ke, G. Ren, F. Zhu, Double-protected zinc ferrite nanospheres as high rate and stable anode materials for lithium ion batteries, J. Power Sources 442 (2019), https://doi.org/10.1016/j.jpowsour.2019.227256.
[7] X. Yao, J. Kong, D. Zhou, C. Zhao, R. Zhou, X. Lu, Mesoporous zinc ferrite/graphene composites: towards ultra-fast and stable anode for lithium-ion batteries, Carbon N. Y. 79 (2014) 493–499, https://doi.org/10.1016/j.carbon.2014.08.007.
[8] M. Bini, M. Ambrosetti, D. Spada, ZnFe2O4, a green and high-capacity anode material for lithium-ion batteries: a review, Appl. Sci. 11 (2021), https://doi.org/10.3390/app112411713.
[9] Y. Ding, Y. Yang, H. Shao, High capacity ZnFe2O4 anode material for lithium ion batteries, Electrochim. Acta 56 (2011) 9433–9438, https://doi.org/10.1016/j.electacta.2011.08.031.
[10] H. Hwang, H. Shin, W.J. Lee, Effects of calcination temperature for rate capability of triple-shelled ZnFe2O4 hollow microspheres for lithium ion battery anodes, Sci. Rep. 7 (2017) 1–10, https://doi.org/10.1038/srep46378.
[11] D. Bresser, F. Mueller, M. Fiedler, S. Krueger, R. Kloepsch, D. Baither, M. Winter, E. Paillard, S. Passerini, Transition-metal-doped zinc oxide nanoparticles as a new lithium-ion anode material, Chem. Mater. 25 (2013) 4977–4985, https://doi.org/10.1021/cm403443t.
[12] G. Wu, Z. Jia, Y. Cheng, H. Zhang, X. Zhou, H. Wu, Easy synthesis of multi-shelled ZnO hollow spheres and their conversion into hedgehog-like ZnO hollow spheres with superior rate performance for lithium ion batteries, Appl. Surf. Sci. 464 (2019) 472–478, https://doi.org/10.1016/j.apsusc.2018.09.115.
[13] T. Liu, Y. Guo, S. Hou, W. Fu, J. Li, L. Meng, C. Mei, L. Zhao, Constructing hierarchical ZnO@C composites using discarded Sprite and Fanta drinks for enhanced lithium storage, Appl. Surf. Sci. 541 (2021) 148495, https://doi.org/10.1016/j.apsusc.2020.148495.
[14] M.V. Reddy, C.Y. Quan, K.W. Teo, L.J. Ho, B.V.R. Chowdari, Mixed oxides, (Ni1-xZnx)Fe2O4 (x = 0, 0.25, 0.5, 0.75, 1): molten salt synthesis, characterization and its lithium-storage performance for lithium ion batteries, J. Phys. Chem. C 119 (2015) 4709–4718, https://doi.org/10.1021/jp5121178.
[15] J. Li, Q. Meng, Y. Zhang, L. Peng, G. Yu, A.C. Marschilok, L. Wu, D. Su, K. J. Takeuchi, E.S. Takeuchi, Y. Zhu, E.A. Stach, Size-dependent kinetics during non-equilibrium lithiation of nano-sized zinc ferrite, Nat. Commun. 10 (2019) 1–8, https://doi.org/10.1038/s41467-018-07831-5.
[16] Longwei Yin, Zhiwei Zhang, Zhaoqiang Li, Hao Fengbin, Qun Li, Chengxiang Wang, Runhua Fan, Yongxin Qi, Spinel ZnMn2O4 nanocrystal-anchored 3D hierarchical carbon aerogel hybrids as anode, Adv. Funct. Mater. 24 (2014) 4176–4185.
[17] Q. Li, Y. Li, W. Jiang, H. Qiu, Y. Zhang, W. He, Preparation and lithium storage properties of zinc ferrite/sulfur-nitrogen co-doped carbon nanotubes composites, Vacuum 222 (2024), https://doi.org/10.1016/j.vacuum.2024.113020.
[18] C. Zhu, D. Chao, J. Sun, I.M. Bacho, Z. Fan, C.F. Ng, X. Xia, H. Huang, H. Zhang, Z. X. Shen, G. Ding, H.J. Fan, Enhanced lithium storage performance of CuO nanowires by coating of graphene quantum dots, Adv. Mater. Interfaces. 2 (2015), https://doi.org/10.1002/admi.201400499.
[19] H. Nan, Y. Zhang, H. Wei, H. Chen, C. Xue, G. Yang, S. Zou, G. Wang, H. Lin, Low-cost and environmentally friendly synthesis of an Al3+ and Mn4+ co-doped Li4Ti5O12 composite with carbon quantum dots as an anode for lithium-ion batteries, RSC Adv. 9 (2019) 22101–22105, https://doi.org/10.1039/c9ra03897c.
[20] B. Jiang, Y. Liang, X. Yu, G. Yuan, M. Zheng, Y. Xiao, H. Dong, Y. Liu, H. Hu, Facile synthesis of FeCO3/nitrogen-doped carbon dot composites for lithium-ion battery anodes, J. Alloys Compd. 838 (2020) 155508, https://doi.org/10.1016/j.jallcom.2020.155508.
[21] M. Krajewski, C.H. Chen, Z.T. Huang, J.Y. Lin, Li4Ti5O12 coated by biomass-derived carbon quantum dots as anode material with enhanced electrochemical performance for lithium-ion batteries, Energies 15 (2022), https://doi.org/10.3390/en15207715.
[22] S. Ravitz Wyngaard, M. Kissinger, Embracing a footprint assessment approach for analyzing desert-based agricultural systems: the case of Medjool dates, Agron, Sustain. Dev. 42 (2022), https://doi.org/10.1007/s13593-022-00802-7.
[23] L. Xu, T. Meng, X. Zheng, T. Li, A.H. Brozena, Y. Mao, Q. Zhang, B.C. Clifford, J. Rao, L. Hu, Nanocellulose-carboxymethylcellulose electrolyte for stable, high-rate zinc-ion batteries, Adv. Funct. Mater. (2023), https://doi.org/10.1002/adfm.202302098.
[24] N.Y. Abu-Thabit, A.A. Judeh, A.S. Hakeem, A. Ul-Hamid, Y. Umar, A. Ahmad, Isolation and characterization of microcrystalline cellulose from date seeds (Phoenix dactylifera L.), Int. J. Biol. Macromol. 155 (2020) 730–739, https://doi.org/10.1016/j.ijbiomac.2020.03.255.
[25] S. Hu, X. Meng, F. Tian, W. Yang, N. Li, C. Xue, J. Yang, Q. Chang, Dual photoluminescence centers from inorganic-salt-functionalized carbon dots for ratiometric pH sensing, J. Mater. Chem. C 5 (2017) 9849–9853, https://doi.org/10.1039/c7tc03266h.
[26] S. Hu, Z. Wei, Q. Chang, A. Trinchi, J. Yang, A facile and green method towards coal-based fluorescent carbon dots with photocatalytic activity, Appl. Surf. Sci. 378 (2016) 402–407, https://doi.org/10.1016/j.apsusc.2016.04.038.
[27] A.R. Bowers, S.H. Cho, A. Singh, Chemical oxidation of aromatic compounds: comparison of H2O2, KMnO4 and O3 for toxicity reduction and improvements in biodegradability, Chem. Oxid (2021) 11–25.
[28] J.S. Hamada, I.B. Hashim, F.A. Sharif, Preliminary analysis and potential uses of date pits in foods, Food Chem. 76 (2002) 135–137, https://doi.org/10.1016/S0308-8146(01)00253-9.
[29] M.E. Babiker, A.R.A. Aziz, M. Heikal, S. Yusup, Pyrolysis characteristics of Phoenix dactylifera date palm seeds using thermo-gravimetric analysis (TGA), Int. J. Environ. Sustain Dev. (2013) 521–524, https://doi.org/10.7763/ijesd.2013.v4.406.
[30] H. Kamal, H.M. Habib, A. Ali, P.L. Show, A.K. Koyande, E. Kheadr, W.H. Ibrahim, Food waste valorization potential: fiber, sugar, and color profiles of 18 date seed varieties (Phoenix dactylifera, L.), J. Saudi Soc. Agric. Sci. 22 (2023) 133–138, https://doi.org/10.1016/j.jssas.2022.11.001.
[31] R.Y. Hong, J.H. Li, H.Z. Li, J. Ding, Y. Zheng, D.G. Wei, Synthesis of Fe3O4 nanoparticles without inert gas protection used as precursors of magnetic fluids, J. Magn. Magn Mater. 320 (2008) 1605–1614, https://doi.org/10.1016/j.jmmm.2008.01.015.
[32] M.Y. Nassar, I.S. Ahmed, T.Y. Mohamed, M. Khatab, A controlled, template-free, and hydrothermal synthesis route to sphere-like α-Fe2O3 nanostructures for textile dye removal, RSC Adv. 6 (2016) 20001–20013, https://doi.org/10.1039/c5ra26112k.
[33] J. Song, S. Baek, S. Lim, Effect of hydrothermal reaction conditions on the optical properties of ZnO nanorods, Phys. B Condens. Matter 403 (2008) 1960–1963, https://doi.org/10.1016/j.physb.2007.10.337.
[34] Q. Wu, Z. Hu, Y. Liu, A novel electrode material of NiO prepared by facile hydrothermal method for electrochemical capacitor application, J. Mater. Eng. Perform. 22 (2013) 2398–2402, https://doi.org/10.1007/s11665-013-0518-y.
[35] K. Velmurugana, V.S.K. Venkatachalapathy, S. Sendhilnathanc, Synthesis of nickel zinc iron nanoparticles by coprecipitation technique, Mater. Res. 13 (2010) 299–303, https://doi.org/10.1590/s1516-14392010000300005.
[36] R. Swaminathan, J. Woods, S. Calvin, J. Huth, M.E. McHenry, Microstructural evolution model of the sintering behaviour and magnetic properties of NiZn ferrite nanoparticles, 11th Int. Ceram. Congr. 45 (2006) 2337–2344. https://doi.org/10.4028/www.scientific.net/ast.45.2337.
[37] L. Li, B. Jin, X. Lang, C. Yang, W. Gao, Y. Zhu, S. Dou, Q. Jiang, Facile synthesis of NixZn1−xFe2O4 (x=0, 0.25, 0.5, 0.75, 1) as anode materials for lithium storage, Chempluschem 81 (2016) 1174–1181, https://doi.org/10.1002/cplu.201600338.
[38] C. Li, W. Liu, F. Jiao, C. Yang, G. Li, S. Liu, W. Qin, Separation and recovery of zinc, lead and iron from electric arc furnace dust by low temperature smelting, Sep. Purif. Technol. 312 (2023) 123355, https://doi.org/10.1016/j.seppur.2023.123355.
[39] Y. Wang, D. Pan, M. Zhang, T. Ma, H. Liu, Z. Yan, J. Xie, Construction of three-dimensional nitrogen-doped graphene coated with uniform nickel oxide/nickel ferrite nanoparticles with enhanced electrochemical properties for supercapacitors, J. Alloys Compd. 765 (2018) 480–488, https://doi.org/10.1016/j.jallcom.2018.06.222.
[40] A.A. Tahir, K.G.U. Wijayantha, Photoelectrochemical water splitting at nanostructured ZnFe 2O 4 electrodes, J. Photochem. Photobiol. Chem. 216 (2010) 119–125, https://doi.org/10.1016/j.jphotochem.2010.07.032.
[41] S. Kumari, R. Sharma, N. Thakur, A. Kumari, Removal of organic and inorganic effluents from wastewater by using degradation and adsorption properties of transition metal-doped nickel ferrite, Environ. Sci. Pollut. Res. 31 (2023) 46526–46545, https://doi.org/10.1007/s11356-023-26567-4.
[42] Y. He, L. Zhang, H.W. Xiong, X. Kang, Evolution of lattice defects in nickel ferrite spinel: oxygen vacancy and cation substitution, J. Alloys Compd. 917 (2022) 165494, https://doi.org/10.1016/j.jallcom.2022.165494.
[43] J.G. Monsalve, C. Ostos, E. Ramos, J.G. Ramírez, O. Arnache, Insight into magnetic properties in zinc ferrite thin films by tuning oxygen content, Curr. Appl. Phys. 22 (2021) 77–83, https://doi.org/10.1016/j.cap.2020.12.015.
[44] S.Y. Song, K.K. Liu, J.Y. Wei, Q. Lou, Y. Shang, C.X. Shan, Deep-ultraviolet emissive carbon nanodots, Nano Lett. 19 (2019) 5553–5561, https://doi.org/10.1021/acs.nanolett.9b02093.
[45] R. Atchudan, T.N.J.I. Edison, Y.R. Lee, Nitrogen-doped carbon dots originating from unripe peach for fluorescent bioimaging and electrocatalytic oxygen reduction reaction, J. Colloid Interface Sci. 482 (2016) 8–18, https://doi.org/10.1016/j.jcis.2016.07.058.
[46] R.B. González-González, L.T. González, M. Madou, C. Leyva-Porras, S.O. Martinez-Chapa, A. Mendoza, Synthesis, purification, and characterization of carbon dots from non-activated and activated pyrolytic carbon black, Nanomaterials 12 (2022), https://doi.org/10.3390/nano12030298.
[47] S. Chandra, V.K. Singh, P.K. Yadav, D. Bano, V. Kumar, V.K. Pandey, M. Talat, S. H. Hasan, Mustard seeds derived fluorescent carbon quantum dots and their peroxidase-like activity for colorimetric detection of H 2 O 2 and ascorbic acid in a real sample, Anal. Chim. Acta 1054 (2019) 145–156, https://doi.org/10.1016/j.aca.2018.12.024.
[48] B. Sankara Reddy, S. Venkatramana Reddy, N. Koteeswara Reddy, Physical and magnetic properties of (Co, Ag) doped ZnO nanoparticles, J. Mater. Sci. Mater. Electron. 24 (2013) 5204–5210, https://doi.org/10.1007/s10854-013-1545-z.
[49] Y.L. Lo, B.J. Hwang, In situ Raman studies on cathodically deposited nickel hydroxide films and electroless Ni-P electrodes in 1 M KOH solution, Langmuir 14 (1998) 944–950, https://doi.org/10.1021/la9600255.
[50] S. Tiwari, R.J. Choudhary, R. Prakash, D.M. Phase, Growth and properties of pulsed laser deposited thin films of Fe 3O4 on Si substrates of different orientation, J. Phys. Condens. Matter 19 (2007), https://doi.org/10.1088/0953-8984/19/17/176002.

[51] A. Jorio, M.M. Lucchese, F. Stavale, E.H.M. Ferreira, M.V.O. Moutinho, R.B. Capaz, C.A. Achete, Raman study of ion-induced defects in N -layer graphene, J. Phys. Condens. Matter 22 (2010), https://doi.org/10.1088/0953-8984/22/33/334204.
[52] P. Yang, J. Zhao, L. Zhang, L. Li, Z. Zhu, Intramolecular hydrogen bonds quench photoluminescence and enhance photocatalytic activity of carbon nanodots, Chem. Eur J. 21 (2015) 8561–8568, https://doi.org/10.1002/chem.201405088.
[53] R.L. Li, Z. Bin Zhao, C.Y. Leng, Y. Li, L.S. Ai, Y. Sun, X.Z. Wang, J.S. Qiu, Preparation of carbon dots from carbonized corncobs by electrochemical oxidation and their application in Na-batteries, Xinxing Tan Cailiao/New Carbon Mater. 38 (2023) 347–355, https://doi.org/10.1016/S1872-5805(22)60644-9.
[54] C. Keller, A. Desrues, S. Karuppiah, E. Martin, J.P. Alper, F. Boismain, C. Villevieille, N. Herlin-Boime, C. Haon, P. Chenevier, Effect of size and shape on electrochemical performance of nano-silicon-based lithium battery, Nanomaterials 11 (2021) 1–15, https://doi.org/10.3390/nano11020307.
[55] Y. Zheng, Y. Li, R. Huang, Y. Huang, J. Yao, B. Huang, A.A. Dubale, Fabrication of 2D NiO porous nanosheets with superior lithium storage performance via a facile thermal-decomposition method, ACS Appl. Energy Mater. 2 (2019) 8262–8273, https://doi.org/10.1021/acsaem.9b01725.
[56] Y. Li, Y. Huang, Y. Zheng, R. Huang, J. Yao, Facile and efficient synthesis of A-Fe2O3 nanocrystals by glucose-assisted thermal decomposition method and its application in lithium ion batteries, J. Power Sources 416 (2019) 62–71, https://doi.org/10.1016/j.jpowsour.2019.01.080.
[57] Q. Wang, X. Hou, S. Liu, Y. Wang, S. Gu, G. Zhou, J. Chai, Rambutan-like Ni0.5Zn0.5Fe2O4 nanospheres with tunable N-doped carbon shell as anode materials for high performance lithium-ion batteries, J. Alloys Compd. 978 (2024) 173529, https://doi.org/10.1016/j.jallcom.2024.173529.
[58] J.J.A. Kreissl, J. Petit, R. Oppermann, P. Cop, T. Gerber, M. Joos, M. Abert, J. Tübke, K. Miyazaki, T. Abe, D. Schröder, Electrochemical lithiation/delithiation of ZnO in 3D-structured electrodes: elucidating the mechanism and the solid electrolyte interphase formation, ACS Appl. Mater. Interfaces 13 (2021) 35625–35638, https://doi.org/10.1021/acsami.1c06135.
[59] R. Song, N. Zhang, H. Dong, P. Wang, H. Ding, J. Wang, S. Li, Self-standing three-dimensional porous NiO/Ni anode materials for high-areal capacity lithium storage, Mater. Des. 215 (2022) 110448, https://doi.org/10.1016/j.matdes.2022.110448.
[60] Q. Tan, X. Kong, X. Guan, C. Wang, B. Xu, Crystallization of zinc oxide quantum dots on graphene sheets as an anode material for lithium ion batteries, CrystEngComm 22 (2019) 320–329, https://doi.org/10.1039/c9ce01285k.
[61] A. Kumar Rai, L. Tuan Anh, C.J. Park, J. Kim, Electrochemical study of NiO nanoparticles electrode for application in rechargeable lithium-ion batteries, Ceram. Int. 39 (2013) 6611–6618, https://doi.org/10.1016/j.ceramint.2013.01.097.